

Epitaxial $\text{Sc}_x\text{Al}_{1-x}\text{N}$ on GaN exhibits attractive high-K dielectric properties

Cite as: Appl. Phys. Lett. **120**, 152901 (2022); doi: 10.1063/5.0075636

Submitted: 17 October 2021 · Accepted: 7 March 2022 ·

Published Online: 11 April 2022



View Online



Export Citation



CrossMark

Joseph Casamento,^{1,a)}  Hyunjea Lee,²  Takuya Maeda,³  Ved Gund,²  Kazuki Nomoto,²  Len van Deurzen,⁴  Wesley Turner,⁵  Patrick Fay,⁵  Sai Mu,⁶  Chris G. Van de Walle,⁶  Amit Lal,²  Huili (Grace) Xing,^{1,2,3}  and Debdeep Jena^{1,2,3} 

AFFILIATIONS

¹Department of Materials Science and Engineering, Cornell University, Ithaca, New York 14853, USA

²School of Electrical & Computer Engineering, Cornell University, Ithaca, New York 14853, USA

³Kavli Institute at Cornell for Nanoscale Science, Cornell University, Ithaca, New York 14853, USA

⁴School of Applied and Engineering Physics, Cornell University, Ithaca, New York 14853, USA

⁵Department of Electrical Engineering, University of Notre Dame, South Bend, Indiana 46556, USA

⁶Materials Department, University of California, Santa Barbara, California 93106-5050, USA

^{a)} Author to whom correspondence should be addressed: jac694@cornell.edu

ABSTRACT

Epitaxial $\text{Sc}_x\text{Al}_{1-x}\text{N}$ thin films of ~ 100 nm thickness grown on metal polar GaN substrates are found to exhibit significantly enhanced relative dielectric permittivity (ϵ_r) values relative to AlN. ϵ_r values of ~ 17 – 21 for Sc mole fractions of 17%–25% ($x = 0.17$ – 0.25) measured electrically by capacitance–voltage measurements indicate that $\text{Sc}_x\text{Al}_{1-x}\text{N}$ has the largest relative dielectric permittivity of any existing nitride material. Since epitaxial $\text{Sc}_x\text{Al}_{1-x}\text{N}$ layers deposited on GaN also exhibit large polarization discontinuity, the heterojunction can exploit the *in situ* high-K dielectric property to extend transistor operation for power electronics and high-speed microwave applications.

Published under an exclusive license by AIP Publishing. <https://doi.org/10.1063/5.0075636>

Currently, wide-bandgap, gallium nitride semiconductor based high electron mobility transistors (HEMTs) use AlGaN/GaN or AlN/GaN heterojunctions to generate high density 2D electron gases (2DEGs) due to the polarization discontinuity. These 2DEGs exhibit high electron mobility—much higher than silicon inversion channels, and simultaneously a wider energy bandgap than silicon that enables a higher breakdown voltage. The combination of high speed and high voltage operation has established the Al(Ga)N/GaN semiconductor system as the leading contender for energy-efficient power electronics and microwave applications for 6G and beyond.¹

The performance limit of GaN HEMTs is currently limited by the properties of the gate barrier layer. For example, though the breakdown electric field of GaN is >3 MV/cm, GaN HEMTs exhibit roughly 1 MV/cm effective breakdown field in large part because of enhanced gate leakage by Fowler–Nordheim tunneling at high drain voltages. This limits the applications of GaN HEMTs in power electronics by restricting the drain voltage. The restricted drain voltage also limits the handling capability of devices in RF applications. Another important aspect is transistor speed. The speed of GaN

HEMTs could be improved if the gate barrier is made thinner to increase the transconductance. The transconductance can be expressed as $g_m \sim C_{gs} \cdot v_{sat}$, where $C_{gs} = \epsilon_b/t_b$ is the gate-source capacitance, ϵ_b is the dielectric constant of the barrier layer, t_b is its thickness, and v_{sat} is the electron saturation velocity in the conducting channel. However, decreasing t_b increases the Fowler–Nordheim tunneling induced gate leakage current exponentially,^{2,3} causing a severe penalty in the breakdown voltage.

This classic transistor design bottleneck can be solved by taking a cue from silicon MOSFET technology: by employing a high-K dielectric barrier layer. Since GaN HEMTs are grown by epitaxial processes, it would be ideal if there was an epitaxial, *in situ* grown high-K dielectric. This would potentially simplify device processing but even more importantly, could avoid well-known problems associated with chemical contamination and interfacial defects. The Fowler–Nordheim gate current can be expressed as $J_{FN} = J_{FN,0} \times \exp[-F_0/F]$, where F is the electric field across the barrier and F_0 is the characteristic tunneling field,^{4,5} which depends on the barrier height and barrier thickness. Accordingly, a thick gate dielectric with higher dielectric permittivity

(“high K ” or high ϵ_r) offers the advantage of decreased electron tunneling and leakage currents without a decrease in the gate capacitance.⁶ In this work, the dielectric constant of epitaxial single-crystalline ~ 100 nm thick $\text{Sc}_x\text{Al}_{1-x}\text{N}$ layers grown on n^+ GaN ($N_d \sim 2 \times 10^{19}/\text{cm}^3$) with $x = 0.17$ – 0.25 is found to exhibit up to 2.4 times larger ϵ_r values than AlN ($\epsilon_r \sim 8.9$).

The $\text{Sc}_x\text{Al}_{1-x}\text{N}/\text{GaN}$ heterostructures discussed in this study were grown by molecular beam epitaxy (MBE) in a Veeco[®] GenXplor system with a base pressure of 10^{-10} Torr on Suzhou Nanonwin[®] conductive n-type bulk GaN substrates. A Sc metal source of nominally 99.9% purity (including C and O impurities) from Ames Laboratory was evaporated from a W crucible using a Telemark[®] electron beam evaporation system integrated with MBE equipment. Sc flux control was achieved with an Inficon[®] electron impact emission spectroscopy (EIES) system by directly measuring the Sc atomic optical emission spectra. Aluminum (99.9999% purity), gallium (99.9999% purity), and silicon (99.9999% purity) were supplied using Knudsen effusion cells. Nitrogen (99.9995% purity) active species were supplied using a Veeco[®] RF UNI-Bulb plasma source with a growth pressure of approximately 10^{-5} Torr. The reported growth temperature is the substrate heater temperature measured by a thermocouple. *In situ* monitoring of film growth was performed using a KSA Instruments reflection high energy electron diffraction (RHEED) apparatus with a Staib electron gun operating at 15 kV and 1.5 A. Post-growth x-ray diffraction (XRD) was performed on a PanAnalytical Empyrean diffractometer at 45 kV, 40 mA with Cu $K\alpha_1$ radiation (1.54057 \AA). Post growth AFM measurements were performed using an Asylum Research Cypher ES system. Capacitance–voltage (CV) measurements were performed on a Cascade Microtech 11000 probe station using Keithley 4200 in an N_2 ambient environment at 500 kHz AC frequency at room temperature on $40 \mu\text{m}$ and larger diameter circular Ti/Au electrodes patterned lithographically. Calibration for CV measurements consisted of an open circuit calibration with the probes floating, a short circuit calibration with probes on the same metal, and a 50Ω impedance calibration with the probes across a 50Ω resistor. CV measurements were performed using a parallel series conductance model to extract the capacitance of the system. Frequency-response measurements were performed using a Keysight E4980E LCR meter and a Keysight 4294A (precision impedance analyzer) using a short/open/load calibration with coaxial on-wafer Kelvin probes.

All $\text{Sc}_x\text{Al}_{1-x}\text{N}/n^+\text{GaN}$ heterostructures for this study were epitaxially grown in a reactive nitrogen environment in the MBE chamber at 200 W RF nitrogen plasma power and 1.95 standard cubic centimeters per minute (sccm) flow rate. The n^+ GaN layers were grown with a Si doping concentration of $\sim 2 \times 10^{19}/\text{cm}^3$ under metal rich conditions with III/V ratio > 1 at 700°C substrate temperature to promote smooth morphologies for the subsequent $\text{Sc}_x\text{Al}_{1-x}\text{N}$ layers and to serve as the conductive bottom electrode. Sc and Al atomic percentages in the film were adjusted by the ratio of the respective fluxes from the effusion cell for Al and E-Beam for Sc. The $\text{Sc}_x\text{Al}_{1-x}\text{N}$ layers were grown under nitrogen rich conditions with III/V ratio ~ 0.85 at a substrate temperature of $\sim 600^\circ\text{C}$. Sc and Al were co deposited continuously during the growth. A more detailed description of the growth and justification for the Sc source selection is described elsewhere,⁷ and the RHEED and AFM data appear in the [supplementary material](#).

Figure 1 shows the XRD scans of the $\text{Sc}_x\text{Al}_{1-x}\text{N}/\text{GaN}$ heterostructures with varying Sc concentrations. An increasing 2θ position

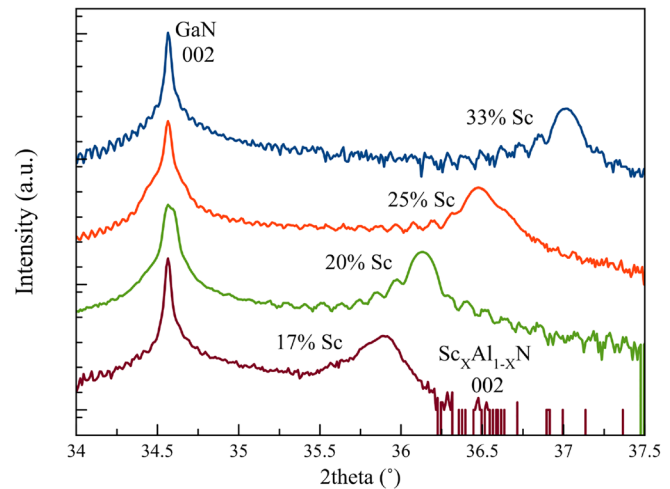


FIG. 1. Symmetric 2Θ - ω x-ray diffraction 002 peak positions for ~ 100 nm thick $\text{Sc}_x\text{Al}_{1-x}\text{N}$ grown on n^+ GaN bulk substrates. The 002 peak position increases as the Sc mole fraction is increased. Sc mole fractions were obtained by comparing peak positions to those of prior $\text{Sc}_x\text{Al}_{1-x}\text{N}$ samples calibrated by Rutherford backscattering.

as the Sc content is increased indicates a decrease in the c -axis lattice parameter. Interference fringes indicate smooth and coherent $\text{Sc}_x\text{Al}_{1-x}\text{N}$ -GaN interfaces. The full-width-half maximum (FWHM) of the 002 peak positions ranges from 0.03° to 0.05° (100 – 180 arc sec). The thickness of the $\text{Sc}_x\text{Al}_{1-x}\text{N}$ layers was verified by x-ray reflectivity (XRR) measurements (not shown). *In situ* RHEED images confirm epitaxial, single-crystalline growth of $\text{Sc}_x\text{Al}_{1-x}\text{N}$.

Figure 2(a) shows the lattice parameter evolution with a Sc content evaluated from x ray with information from prior $\text{Sc}_x\text{Al}_{1-x}\text{N}$ samples grown at the same deposition conditions (e.g., III/V ratio, substrate temperature) calibrated by prior Rutherford backscattering (RBS) measurements. Figure 2(b) shows the wurtzite crystal structure of AlN and the a and c -axis lattice parameters: Sc substitutes the Al sites. Energy dispersive spectroscopy (EDS) results from scanning electron microscopy (SEM) obtained Sc mole fractions that were similar (within 2 atomic %) to the Sc mole fractions mentioned. The uncertainty in the Sc content is $\pm 4.5\%$ for SEM-EDS and $\pm 2\%$ for RBS. The Sc mole fractions were independently calibrated using Rutherford backscattering. A non-monotonic trend of the c -axis lattice parameter with Sc mole fraction is seen. This trend cannot be explained from epitaxial strain alone. The in-plane lattice parameter (a axis) of $\text{Sc}_x\text{Al}_{1-x}\text{N}$ at higher Sc mole fractions ($x > 0.18$) is larger than that of GaN. Accordingly, $\text{Sc}_x\text{Al}_{1-x}\text{N}$ films would be under compressive strain and cause the in-plane lattice parameter to effectively decrease. A positive Poisson ratio would then cause the out of plane lattice parameter (c axis) to increase. The opposite is true for $\text{Sc}_x\text{Al}_{1-x}\text{N}$ at lower Sc mole fractions ($x < 0.18$), where a tensile strain to GaN would cause the in-plane lattice parameter to effectively increase and the out-of-plane lattice parameter to effectively decrease. Thus, the observed experimental trend is opposite of strain-based expectation.

A possible reason for the non-monotonic trend is the competition between an increasing average bond length as more Sc is incorporated into tetrahedral sites and structural distortion that tilts the

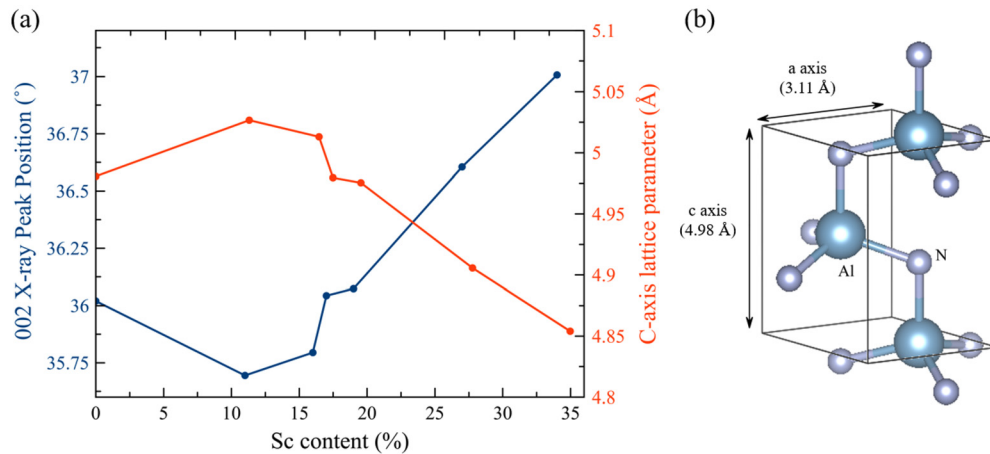


FIG. 2. (a) Symmetric $2\theta-\omega$ XRD 002 peak positions for $\text{Sc}_x\text{Al}_{1-x}\text{N}$ and the corresponding calculated c-axis lattice parameters. The non-monotonic trend of the c-axis lattice parameter with a Sc content is observed. (b) Ball and stick crystal structure model of the wurtzite unit cell of AlN, showing the relative a and c axis orientations.

tetrahedra away from the c-axis as more Sc is incorporated.^{8,9} The increasing average bond length acts to increase the c-axis lattice parameter. The structural distortion that decreases the projection of the bonds onto the c-axis acts to decrease the c-axis lattice parameter. This non-monotonic behavior and deviation from Vegard's law is related to the fact that rock salt ScN is more thermodynamically stable than wurtzite ScN.^{10–13} Accordingly, $\text{Sc}_x\text{Al}_{1-x}\text{N}$ can be viewed as a balance between competing tetrahedral coordination in wurtzite AlN

and octahedral coordination in rock salt ScN. Similar behavior is also predicted to occur for $\text{Y}_x\text{Al}_{1-x}\text{N}$ ¹⁴ and when alloying other transition metals into AlN. This non-monotonic behavior is not observed in $\text{Al}_x\text{Ga}_{1-x}\text{N}$ and $\text{In}_x\text{Al}_{1-x}\text{N}$ alloy systems, because the endmember binary semiconductors GaN and InN have thermodynamically stable wurtzite crystal structures.

Figure 3 shows the 500 kHz CV results for samples with three Sc mole fractions studied in a capacitor geometry, where the underlying

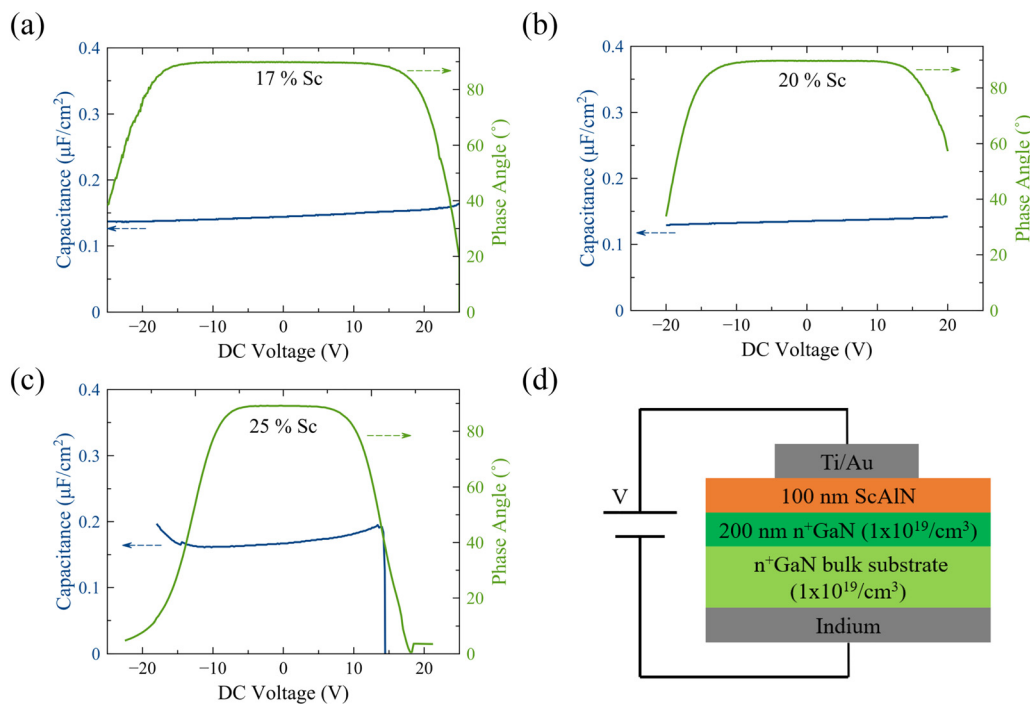


FIG. 3. (a)–(c) CV data at 500 kHz frequency showing the capacitance per unit area and phase angle of Sc contents 17%–25% ($x = 0.17$ – 0.25) in $\text{Sc}_x\text{Al}_{1-x}\text{N}$ for $40\ \mu\text{m}$ diameter circular electrodes. (d) Schematic of the heterostructure configuration for CV measurements.

n^+ GaN serves as an epitaxial bottom electrode. As indicated in the figure, Ti/Al top metal electrodes were patterned by optical lithography, and indium was adhered to the backside of the n^+ GaN substrate to serve as a bottom contact for vertical measurements. A relatively constant capacitance value with a small positive slope indicates uniform and high n type (donor) doping levels in the conductive n^+ GaN layer. The figure also shows the phase angle between the real (conductance) and imaginary (capacitance) parts of impedance where 90° indicates low conductance. For the three Sc compositions measured (17%–25% Sc), the capacitance values are roughly constant across a voltage range that corresponds to average electric fields of $\sim 1.0\text{--}1.5\text{ MV/cm}$ within which the capacitance can be extracted. The drop in the phase angle below 90° at elevated voltages occurs due to the onset of electrical leakage: the leakage increases with the Sc mole fraction.

Figure 4 shows the measured frequency dependence of ϵ_r from 1 kHz to 20 MHz, as extracted from on-wafer capacitance measurements. As can be seen, ϵ_r ranges from ~ 15 to 20 for the three Sc compositions characterized. The values agree with those shown at 500 kHz (Fig. 3) and indicate that space charge polarization does not significantly influence the ϵ_r values at higher measurement frequencies. It should be noted that the 17% and 20% samples show a constant capacitance over the full range of frequencies measured; the modest apparent frequency dependence seen for the 25% composition devices is a result of the increased effective conductance due to defects in $\text{Sc}_x\text{Al}_{1-x}\text{N}$ layers with higher Sc mole fractions (as indicated by the larger deviation from the 90° phase at low frequencies).

A summary of CV measurement results for several Ti/Au electrode sizes is included in Table I. The measured ϵ_r values are relatively consistent across multiple electrode sizes, indicating the reliability of the measurements and the ability to probe large diameter electrodes without significant electrical leakage at low applied voltages. For $40\ \mu\text{m}$ diameter electrodes, the nominal phase angles reported correspond to loss tangent ($\tan \delta$) values of 0.002, 0.003, and 0.016 for 17%, 20%, and 25% Sc, respectively. These loss tangent values are comparable to those obtained from sputter deposited $\text{Sc}_x\text{Al}_{1-x}\text{N}$ and can be

improved upon. The $\epsilon_r \sim 15\text{--}20$ values establish epitaxial $\text{Sc}_x\text{Al}_{1-x}\text{N}$ as a high-K dielectric material with $\sim 2\text{X}$ higher dielectric constant than AlN, GaN, or their alloys.¹⁵

Sc has a larger atomic radius than Al and a larger electronic polarizability. The increase in ϵ_r is, thus, expected when Sc is added due to decreased nuclear shielding from the core electrons. Also, the ionic polarizability of Sc^{+3} is larger than that of Al^{+3} ,¹⁶ partially due to the smaller electronegativity of Sc^{+3} . A smaller cation electronegativity implies that the outermost shell experiences a weaker attractive force on neighboring anion electrons in accordance with increased polarizability. Cation ionic polarizability is dependent on the specific crystal environment of the cation (e.g., unit cell volume, corresponding anion), so quantitative values are not easily determined. Nevertheless, these qualitative trends suggest that isoelectronic alloying of Sc^{+3} on tetrahedral sites in the wurtzite unit cell should increase the polarizability of the crystal.

The measured ϵ_r values in this report are similar to those obtained in sputter deposited $\text{Sc}_x\text{Al}_{1-x}\text{N}$ films and predicted values.^{17–30}

To further elucidate the observed enhancement in ϵ_r , we performed density functional calculations for a $\text{Sc}_x\text{Al}_{1-x}\text{N}$ alloy at 16.7% Sc using the perturbation theory. The disordered environment of the alloy was simulated using ten different 108-atom supercells with nine Sc atoms randomly distributed over the 54 cation sites in each supercell. We used projector augmented wave potentials³¹ as implemented in the Vienna *ab initio* simulation package (VASP)^{32,33} and a plane wave energy cutoff of 500 eV. Exchange and correlation were treated in the generalized gradient approximation.³⁴ The Γ point was used for Brillouin-zone integration, and the structure was fully optimized with final Hellmann–Feynman forces less than 5 meV.

We found that the electronic part and the in-plane components of the ionic part of the dielectric constant did not change much relative to pure AlN. In contrast, the out-of-plane component of the ionic part exhibited a notable increase with values in different supercells ranging from 15 to 30. This enhancement can be attributed to bond softening

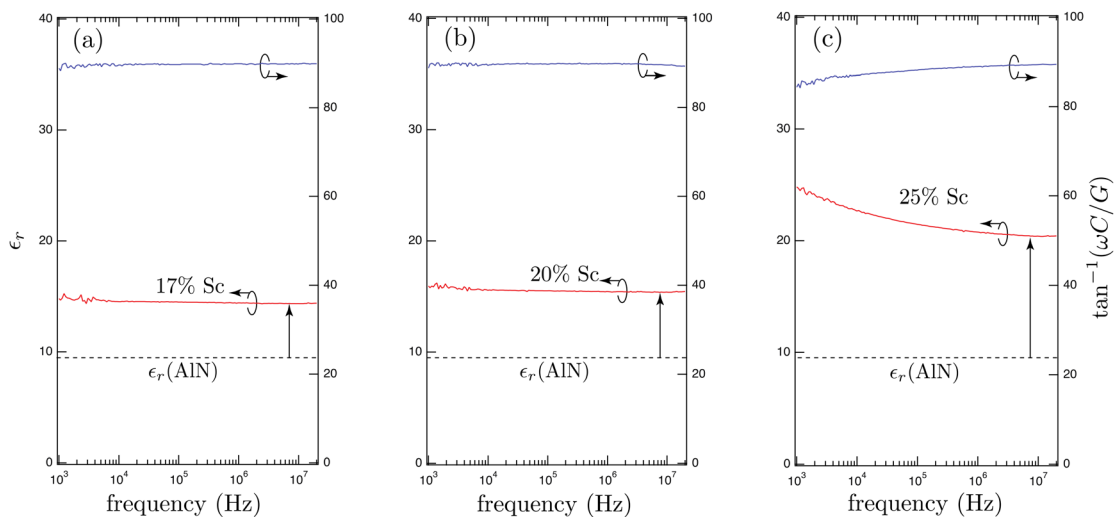


FIG. 4. (a)–(c) Extracted relative dielectric permittivity (ϵ_r) at multiple measurement frequencies. The dispersion seen for the 25% Sc sample is indicative of space charge polarization at very low measurement frequencies. The values at 500 kHz frequency agree with the prior results in this paper.

TABLE I. Extracted dielectric permittivity (ϵ_r) for $\text{Sc}_x\text{Al}_{1-x}\text{N-n}^+\text{GaN}$ heterostructures and measured phase angle ($^\circ$) at low voltages from CV measurements as a function of the Sc content and metal electrode diameter (d). Measurements were conducted at 500 kHz frequency. Values for 33% Sc are not shown as the phase angle deviates significantly from 90° due to electrical leakage. Note that the ϵ_r for AlN is ~ 8.9 .¹⁵

Sc content	Parameters	d = 40 μm	d = 80 μm	d = 135 μm
17%	ϵ_r	17	16	15
	θ ($^\circ$)	-89.85	-89.95	-89.60
20%	ϵ_r	15	15	15
	θ ($^\circ$)	-89.83	-89.67	-89.64
25%	ϵ_r	22	21	21
	θ ($^\circ$)	-89.06	-89.09	-88.65

along the c direction in the $\text{Sc}_x\text{Al}_{1-x}\text{N}$ alloy,³⁵ which we confirmed by a crystal orbital Hamilton population analysis^{36,37} (see Fig. 5). With softer out-of-plane bonds, an electric field along the c axis induces larger atomic displacement and polarization change, giving rise to the enhanced dielectric response. Averaging the dielectric constant (including both electric and ionic contributions) over three Cartesian directions and over ten supercells, we found a value of 15.0 in satisfactory agreement with the experimental measurement at 17% Sc.

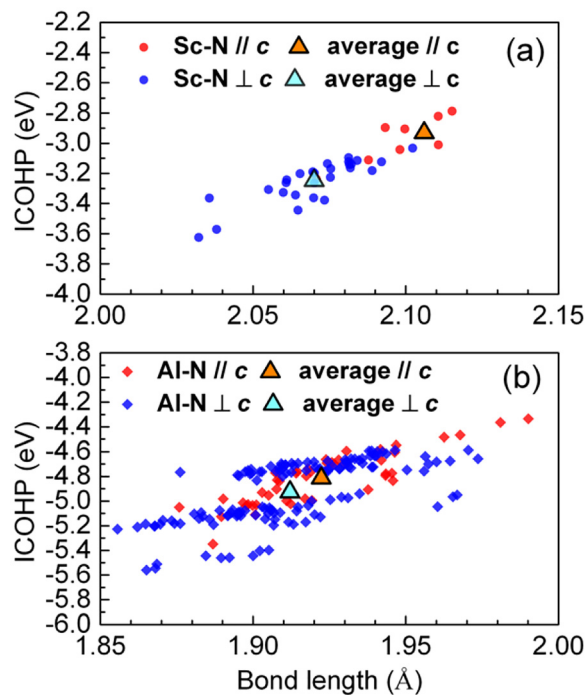


FIG. 5. Integrated (over occupied states) crystal orbital Hamilton populations (ICOHP) for each cation–anion interaction in a 108-atom $\text{Sc}_x\text{Al}_{1-x}\text{N}$ ($x = 16.7\%$) supercell as a function of the bond length: (a) Sc–N bonds (circles) and (b) Al–N bonds (diamonds). Red and blue distinguish bonds along the c axis in the buckled plane. Averages are denoted using triangles. ICOHP is an indicator of the bonding strength: the more negative values yield stronger bonds. The magnitude of the averaged ICOHP for Sc–N bonds along the c axis becomes smaller than that for the in-plane Sc–N bonds or for the Al–N bonds, indicating softer Sc–N bonds along the c axis.

Figure 6 shows a comparison between the low frequency relative dielectric permittivity of common III-nitride semiconductors and dielectrics used for III-nitride electronic and photonic devices. $\text{Sc}_x\text{Al}_{1-x}\text{N}$ ($x = 0.25$) has an ϵ_r value that is the highest of any existing III-nitride material ($\epsilon_r \sim 21$) and comparable with other dielectrics such as HfO_2 and Ta_2O_5 . Though the ϵ_r value for InN is ~ 15 , the relatively low bandgap and conductive nature of InN has precluded its use as a dielectric material; $\text{Sc}_x\text{Al}_{1-x}\text{N}$ does not suffer from these drawbacks. Since optical absorption measurements for bandgaps could not be performed directly on the $\text{Sc}_x\text{Al}_{1-x}\text{N}$ -GaN heterostructures due to the smaller bandgap of GaN, films of $\text{Sc}_x\text{Al}_{1-x}\text{N}$ ($0.0 < x < 0.25$) of ~ 200 nm thicknesses were separately grown on AlN on c -plane sapphire substrates with the same conditions (e.g., III/V ratio, temperature) as those grown on $n^+\text{GaN}$ discussed earlier. They show near optical absorption edges ranging from 6.0 to 5.1 eV (not shown). The bandgaps of $\text{Sc}_x\text{Al}_{1-x}\text{N}$ on AlN seen here are similar to prior reports for sputter deposited and MBE grown $\text{Sc}_x\text{Al}_{1-x}\text{N}$ at a similar Sc content.^{39,40} Assuming the bandgap of $\text{Sc}_x\text{Al}_{1-x}\text{N}$ is the same when grown on AlN and GaN, this gives $\text{Sc}_x\text{Al}_{1-x}\text{N}$ a relatively large bandgap and relative dielectric permittivity. A commonly reported hi-K metric is the “equivalent oxide thickness” or EOT, which is defined relative to the SiO_2 dielectric thickness that has a low frequency $\epsilon_r \sim 3.9$. Namely, a higher relative dielectric permittivity oxide material has a lower equivalent oxide thickness and is, therefore, attractive for vertical scaling of nitride HEMTs. Here, the term can be extended to hi-K nitride dielectrics like $\text{Sc}_x\text{Al}_{1-x}\text{N}$, as an “equivalent nitride thickness” with a comparison to $\text{Al}(\text{Ga})\text{N}$, or a Si_3N_4 dielectric thickness with a low-frequency ϵ_r of ~ 7.5 .

Furthermore, most dielectric materials are deposited by *ex situ* deposition techniques and/or in a non-epitaxial manner. For example, polycrystalline and/or amorphous Al_2O_3 , SiO_2 , and Si_3N_4 deposited *ex situ* are typically used in GaN HEMTs, requiring air-exposure and loss of control of surface and interfacial properties.⁴¹ Since sputter deposited $\text{Sc}_x\text{Al}_{1-x}\text{N}$ on metal electrodes has also shown enhanced

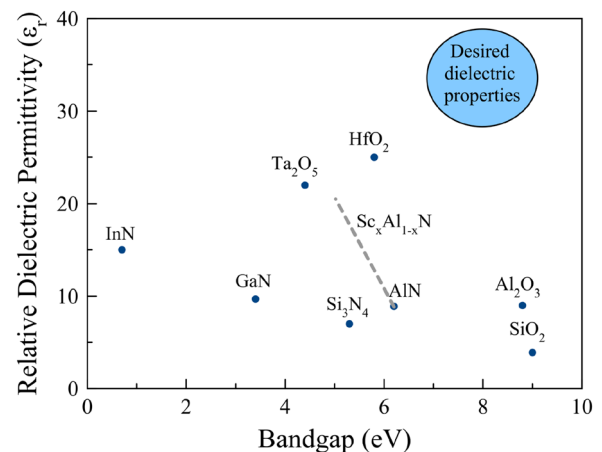


FIG. 6. Comparison of low frequency relative dielectric permittivity and optical bandgap of common III-nitride semiconductors and dielectric materials utilized for III-nitride materials. Several data points were taken from Ref. 38. The results for various Sc mole fraction $\text{Sc}_x\text{Al}_{1-x}\text{N}$ discussed here are indicated along the dashed line. The $\text{Sc}_x\text{Al}_{1-x}\text{N}$ bandgap value used is from separate $\text{Sc}_x\text{Al}_{1-x}\text{N}$ samples grown on AlN on c -plane sapphire templates.

piezoelectric and ferroelectric properties,^{42–54} one could potentially avail of these properties in addition to the high-K since it is now a complementary metal oxide semiconductor (CMOS) compatible material due to the utilization of relatively low deposition temperatures and large wafer scale production of bulk acoustic wave filters.^{55,56} However, as discussed earlier, *in situ* deposition of $\text{Sc}_x\text{Al}_{1-x}\text{N}$ on the transistor channel potentially eliminates surface contamination and can be performed in the same epitaxial tools used to deposit AlN and GaN HEMT thin films such as MBE or MOCVD. Epitaxial growth of $\text{Sc}_x\text{Al}_{1-x}\text{N}$ via MBE and MOCVD on semiconducting layers such as GaN, AlN, and SiC has seen increased attention and development in recent years^{39,57–72} with enhanced piezoelectricity and even ferroelectric behavior seen in MBE films.^{73–75} Analogies for $\text{Sc}_x\text{Al}_{1-x}\text{N}$ on GaN may be drawn here⁵⁵ with the development of hi-K HfO_2 for silicon CMOS and subsequent discovery of ferroelectricity in $(\text{HfZr})\text{O}_2$. Notably, $\text{Sc}_x\text{Al}_{1-x}\text{N}$ is lattice-matched to the in-plane lattice parameter of GaN at $x \sim 0.18$, making epitaxial stabilization of wurtzite $\text{Sc}_x\text{Al}_{1-x}\text{N}$ with tunable thicknesses on GaN possible. This is highly desirable as AlN grown on GaN forms cracks along the hexagonal unit cell axes at $\sim 6\text{--}7$ nm thicknesses to relieve the tensile misfit strain.⁷⁶ In contrast to sputter deposition, MBE typically produces high crystal quality at ultra-thin thicknesses and is attractive for precise thickness control and near elimination of chemical contamination of heterojunction interfaces, where mobile carriers reside in the transistor channels.

In conclusion, insight into the lattice parameter evolution of $\text{Sc}_x\text{Al}_{1-x}\text{N}$ grown epitaxially on GaN is obtained with a trend of decreasing c-axis lattice parameter values once the Sc content is increased past the nominally lattice-matched composition of $\sim 18\%$ Sc ($x = 0.18$). The relative dielectric permittivity increases as the Sc content is increased, reaching a value of ~ 21 at $\sim 25\%$ Sc ($x = 0.25$), a value that is competitive with some existing high-K dielectric materials. The realization of an enhanced ϵ_r in $\text{Sc}_x\text{Al}_{1-x}\text{N}$ grown by MBE on GaN paves the way for the potential usage of $\text{Sc}_x\text{Al}_{1-x}\text{N}$ as an epitaxial *in situ* grown dielectric material that can utilize the unique properties and functionality of the $\text{Sc}_x\text{Al}_{1-x}\text{N}$ materials system. This can lead to increased performance of nitride HEMTs by increasing the breakdown voltage and decreasing the tunneling current density through reducing the electric field due to the high-K properties of $\text{Sc}_x\text{Al}_{1-x}\text{N}$.

See the [supplementary material](#) for *in situ* RHEED images, *ex situ* AFM images, and of the films.

This work was supported by the DARPA Tunable Ferroelectric Nitrides (TUFEN) program monitored by Dr. Ronald G. Polcawich. This work was also supported in part by NSF DMREF (Grant No. 1534303); Cornell's nanoscale facility (Grant No. NCCI-1542081); AFOSR (Grant No. FA9550-20-1-0148); NSF (No. DMR-1710298); and the Cornell Center for Materials Research Shared Facilities, which are supported through the NSF MRSEC program (No. DMR-1719875). S.M. was supported by the U.S. Department of Energy, Office of Science, National Quantum Information Science Research Centers, Co-design Center for Quantum Advantage (C2QA) under contract number DE-SC0012704. This work used the Extreme Science and Engineering Discovery Environment (XSEDE), which is supported by NSF under Grant No. ACI1548562. The authors would like to acknowledge the Materials Preparation Center, Ames Laboratory, U.S. DOE Basic Energy

Sciences, Ames, IA, USA for supplying the Sc source material. The authors would also like to acknowledge Professor Darrell Schlom for helpful discussions.

AUTHOR DECLARATIONS

Conflict of Interest

The authors have no conflicts to disclose.

DATA AVAILABILITY

The data that support the findings of this study are available from the corresponding author upon reasonable request.

REFERENCES

- ¹High-Frequency GaN Electronic Devices, edited by P. Fay, D. Jena, and P. Maki (Springer, 2019).
- ²J. Robertson, *Rep. Prog. Phys.* **69**, 327 (2006).
- ³C.-H. Lee, S.-H. Hur, Y.-C. Shin, J.-H. Choi, D.-G. Park, and K. Kim, *Appl. Phys. Lett.* **86**, 152908 (2005).
- ⁴R. H. Fowler and L. W. Nordheim, *Proc. R. Soc. London, Ser. A* **119**, 173 (1928).
- ⁵L. W. Nordheim, *Proc. R. Soc. London, Ser. A* **121**, 626 (1928).
- ⁶A. I. Kingon, J.-P. Maria, and S. K. Streiffer, *Nature* **406**, 1032 (2000).
- ⁷J. Casamento, H. Lee, C. S. Chang, M. F. Besser, T. Maeda, D. A. Muller, H. G. Xing, and D. Jena, *APL Mater.* **9**, 091106 (2021).
- ⁸D. F. Urban, O. Ambacher, and C. Elsässer, *Phys. Rev. B* **103**, 115204 (2021).
- ⁹N. Kurz, A. Ding, D. F. Urban, Y. Lu, L. Kirste, N. M. Feil, A. Žukauskaitė, and O. Ambacher, *J. Appl. Phys.* **126**, 075106 (2019).
- ¹⁰N. Farrer and L. Bellaiche, *Phys. Rev. B* **66**, 201203(R) (2002).
- ¹¹V. Ranjan, L. Bellaiche, and E. J. Walter, *Phys. Rev. Lett.* **90**, 257602 (2003).
- ¹²A. Qteish, P. Rinke, M. Scheffler, and J. Neugebauer, *Phys. Rev. B* **74**, 245208 (2006).
- ¹³J. Casamento, J. Wright, R. Chaudhuri, H. Xing, and D. Jena, *Appl. Phys. Lett.* **115**, 172101 (2019).
- ¹⁴S. Manna, G. L. Brennecke, V. Stevanović, and C. V. Ciobanu, *J. Appl. Phys.* **122**, 105101 (2017).
- ¹⁵G. Yu, in *Properties of Advanced Semiconductor Materials GaN, AlN, InN, BN, SiC, SiGe*, edited by M. E. Levinshtein, S. L. Rumyantsev, and M. S. Shur (John Wiley & Sons, Inc., New York, 2001), pp. 31–47.
- ¹⁶R. D. Shannon, *J. Appl. Phys.* **73**, 348 (1993).
- ¹⁷A. Mazzalai and B. Heinz, in *2018 IEEE International Ultrasonics Symposium (IUS)* (IEEE, 2018), pp. 1–2.
- ¹⁸M. Pirro, B. Herrera, M. Assylbekova, G. Giribaldi, L. Colombo, and M. Rinaldi, in *2021 IEEE 34th International Conference on Micro Electro Mechanical Systems (MEMS)* (IEEE, Gainesville, FL, 2021), pp. 646–649.
- ¹⁹J. Wang, M. Park, S. Mertin, T. Pensala, F. Ayazi, and A. Ansari, *J. Microelectromech. Syst.* **29**, 741 (2020).
- ²⁰S. Mertin, C. Nyffeler, T. Makkonen, B. Heinz, A. Mazzalai, in T. Schmitz-Kempen, S. Tiedke, T. Pensala, and P. Mural, *2019 IEEE International Ultrasonics Symposium (IUS)* (IEEE, Glasgow, 2019), pp. 2592–2595.
- ²¹M. Moreira, J. Bjurström, I. Katarđjević, and V. Yantchev, *Vacuum* **86**, 23 (2011).
- ²²R. Matloub, M. Hadad, A. Mazzalai, N. Chidambaram, G. Moulard, C. S. Sandu, T. Metzger, and P. Mural, *Appl. Phys. Lett.* **102**, 152903 (2013).
- ²³Q. Wang, Y. Lu, S. Mishin, Y. Oshmyansky, and D. A. Horsley, *J. Microelectromech. Syst.* **26**, 1132 (2017).
- ²⁴R. H. Olsson, Z. Tang, and M. D'Agati, in *2020 IEEE Custom Integrated Circuits Conference* (IEEE, Boston, MA, 2020), pp. 1–6.
- ²⁵M. Akiyama, K. Umeda, A. Honda, and T. Nagase, *Appl. Phys. Lett.* **102**, 021915 (2013).
- ²⁶G. Wingqvist, F. Tasnádi, A. Zukauskaite, J. Birch, H. Arwin, and L. Hultman, *Appl. Phys. Lett.* **97**, 112902 (2010).
- ²⁷T. Yanagitani and M. Suzuki, *Appl. Phys. Lett.* **105**, 122907 (2014).
- ²⁸K. Umeda, H. Kawai, A. Honda, M. Akiyama, T. Kato, and T. Fukura, in *2013 IEEE 26th International Conference on Micro Electro Mechanical Systems (MEMS)* (IEEE, Taipei, 2013), pp. 733–736.

- ²⁹Y. Zhang, W. Zhu, D. Zhou, Y. Yang, and C. Yang, *J. Mater. Sci.: Mater. Electron.* **26**, 472 (2015).
- ³⁰O. Ambacher, B. Christian, N. Feil, D. F. Urban, C. Elsässer, M. Prescher, and L. Kirste, *J. Appl. Phys.* **130**, 045102 (2021).
- ³¹P. E. Blöchl, *Phys. Rev. B* **50**, 17953 (1994).
- ³²G. Kresse and J. Hafner, *Phys. Rev. B* **48**, 13115 (1993).
- ³³G. Kresse and J. Furthmüller, *Phys. Rev. B* **54**, 11169 (1996).
- ³⁴J. Perdew, K. Burke, and M. Ernzerhof, *Phys. Rev. Lett.* **77**, 3865 (1996).
- ³⁵F. Tasnádi, B. Alling, C. Höglund, G. Wingqvist, J. Birch, L. Hultman, and I. A. Abrikosov, *Phys. Rev. Lett.* **104**, 137601 (2010).
- ³⁶R. Dronskowski and P. E. Blöchl, *J. Phys. Chem.* **97**, 8617 (1993).
- ³⁷S. Maintz, V. L. Deringer, A. L. Tchougréeff, and R. Dronskowski, *J. Comput. Chem.* **37**, 1030 (2016).
- ³⁸J. Robertson, *J. Vac. Sci. Technol., B: Microelectron. Nanometer Struct.—Process., Meas., Phenom.* **18**, 1785 (2000).
- ³⁹P. Wang, D. A. Laleyan, A. Pandey, Y. Sun, and Z. Mi, *Appl. Phys. Lett.* **116**, 151903 (2020).
- ⁴⁰M. Baeumler, Y. Lu, N. Kurz, L. Kirste, M. Prescher, T. Christoph, J. Wagner, A. Žukauskaitė, and O. Ambacher, *J. Appl. Phys.* **126**, 045715 (2019).
- ⁴¹G. D. Wilk, R. M. Wallace, and J. M. Anthony, *J. Appl. Phys.* **89**, 5243 (2001).
- ⁴²K. Yazawa, D. Drury, A. Zakutayev, and G. L. Brenneka, *Appl. Phys. Lett.* **118**, 162903 (2021).
- ⁴³D. Drury, K. Yazawa, A. Mis, K. Talley, A. Zakutayev, and G. L. Brenneka, *Phys. Status Solidi RRL* **15**, 2100043 (2021).
- ⁴⁴S. Yasuoka, T. Shimizu, A. Tateyama, M. Uehara, H. Yamada, M. Akiyama, Y. Hiranaga, Y. Cho, and H. Funakubo, *J. Appl. Phys.* **128**, 114103 (2020).
- ⁴⁵D. Wang, J. Zheng, P. Musavigharavi, W. Zhu, A. C. Foucher, S. E. Trolrier-McKinstry, E. A. Stach, and R. H. Olsson, *IEEE Electron Device Lett.* **41**, 1774 (2020).
- ⁴⁶S. Fichtner, N. Wolff, F. Lofink, L. Kienle, and B. Wagner, *J. Appl. Phys.* **125**, 114103 (2019).
- ⁴⁷S. Bette, S. Fichtner, S. Bröker, L. Nielen, T. Schmitz-Kempen, B. Wagner, C. Van Buggenhout, S. Tiedke, and S. Tappertzshofen, *Thin Solid Films* **692**, 137623 (2019).
- ⁴⁸N. Kurz, Y. Lu, L. Kirste, M. Reusch, A. Žukauskaitė, V. Lebedev, and O. Ambacher, *Phys. Status Solidi A* **215**, 1700831 (2018).
- ⁴⁹M. A. Caro, S. Zhang, T. Riekkinen, M. Ylilammi, M. A. Moram, O. Lopez-Acevedo, J. Molarius, and T. Laurila, *J. Phys.: Condens. Matter* **27**, 245901 (2015).
- ⁵⁰M. Akiyama, T. Kamohara, K. Kano, A. Teshigahara, Y. Takeuchi, and N. Kawahara, *Adv. Mater.* **21**, 593 (2009).
- ⁵¹M. Akiyama, K. Kano, and A. Teshigahara, *Appl. Phys. Lett.* **95**, 162107 (2009).
- ⁵²Y. Lu, M. Reusch, N. Kurz, A. Ding, T. Christoph, M. Prescher, L. Kirste, O. Ambacher, and A. Žukauskaitė, *APL Mater.* **6**, 076105 (2018).
- ⁵³Y. Song, C. Perez, G. Esteves, J. S. Lundh, C. B. Saltonstall, T. E. Beechem, J. I. Yang, K. Ferri, J. E. Brown, Z. Tang, J.-P. Maria, D. W. Snyder, R. H. Olsson, B. A. Griffin, S. E. Trolrier-McKinstry, B. M. Foley, and S. Choi, *ACS Appl. Mater. Interfaces* **13**, 19031 (2021).
- ⁵⁴M. Islam, N. Wolff, M. Yassine, G. Schönweger, B. Christian, H. Kohlstedt, O. Ambacher, F. Lofink, L. Kienle, and S. Fichtner, *Appl. Phys. Lett.* **118**, 232905 (2021).
- ⁵⁵T. Mikolajick, S. Slesazek, H. Mulaosmanovic, M. H. Park, S. Fichtner, P. D. Lomenzo, M. Hoffmann, and U. Schroeder, *J. Appl. Phys.* **129**, 100901 (2021).
- ⁵⁶V. V. Felmetsger, in *2017 IEEE International Ultrasonics Symposium (IUS)* (IEEE, Washington, DC, 2017), pp. 1–5.
- ⁵⁷M. T. Hardy, E. N. Jin, N. Nepal, D. S. Katzer, B. P. Downey, V. J. Gokhale, D. F. Storm, and D. J. Meyer, *Appl. Phys. Express* **13**, 065509 (2020).
- ⁵⁸K. Frei, R. Trejo-Hernández, S. Schütt, L. Kirste, M. Prescher, R. Aidam, S. Müller, P. Waltereit, O. Ambacher, and M. Fiederle, *Jpn. J. Appl. Phys.* **58**, SC1045 (2019).
- ⁵⁹M. T. Hardy, B. P. Downey, N. Nepal, D. F. Storm, D. S. Katzer, and D. J. Meyer, *Appl. Phys. Lett.* **110**, 162104 (2017).
- ⁶⁰R. Dargis, A. Clark, A. Ansari, Z. Hao, M. Park, D. Kim, R. Yanka, R. Hammond, M. Debnath, and R. Pelzel, *Phys. Status Solidi A* **217**, 1900813 (2020).
- ⁶¹T. E. Kazior, E. M. Chumbes, B. Schultz, J. Logan, D. J. Meyer, and M. T. Hardy, in *2019 IEEE MTT-S International Microwave Symposium (IMS)* (IEEE, Boston, MA, 2019), pp. 1136–1139.
- ⁶²A. J. Green, J. K. Gillespie, R. C. Fitch, D. E. Walker, M. Lindquist, A. Crespo, D. Brooks, E. Beam, A. Xie, V. Kumar, J. Jimenez, C. Lee, Y. Cao, K. D. Chabak, and G. H. Jessen, *IEEE Electron Device Lett.* **40**, 1056 (2019).
- ⁶³M. Park, Z. Hao, D. G. Kim, A. Clark, R. Dargis, and A. Ansari, in *2019 20th International Conference on Solid-State Sensors, Actuators and Microsystems & Eurosensors XXXIII (Transducers Eurosensors XXXIII)* (IEEE, Berlin, 2019), pp. 450–453.
- ⁶⁴A. Ansari, in *2019 IEEE MTT-S International Wireless Symposium (IWS)* (IEEE, Guangzhou, 2019), pp. 1–3.
- ⁶⁵J. Ligl, S. Leone, C. Manz, L. Kirste, P. Doering, T. Fuchs, M. Prescher, and O. Ambacher, *J. Appl. Phys.* **127**, 195704 (2020).
- ⁶⁶S. Leone, J. Ligl, C. Manz, L. Kirste, T. Fuchs, H. Menner, M. Prescher, J. Wiegert, A. Žukauskaitė, R. Quay, and O. Ambacher, *Phys. Status Solidi RRL* **14**, 1900535 (2020).
- ⁶⁷E. N. Jin, M. T. Hardy, A. L. Mock, J. L. Lyons, A. R. Kramer, M. J. Tadjer, N. Nepal, D. S. Katzer, and D. J. Meyer, *ACS Appl. Mater. Interfaces* **12**, 52192 (2020).
- ⁶⁸M. Park, Z. Hao, R. Dargis, A. Clark, and A. Ansari, *J. Microelectromech. Syst.* **29**, 490 (2020).
- ⁶⁹P. Wang, B. Wang, D. A. Laleyan, A. Pandey, Y. Wu, Y. Sun, X. Liu, Z. Deng, E. Kioupakis, and Z. Mi, *Appl. Phys. Lett.* **118**, 032102 (2021).
- ⁷⁰A. L. Mock, A. G. Jacobs, E. N. Jin, M. T. Hardy, and M. J. Tadjer, *Appl. Phys. Lett.* **117**, 232107 (2020).
- ⁷¹C. Manz, S. Leone, L. Kirste, J. Ligl, K. Frei, T. Fuchs, M. Prescher, P. Waltereit, M. A. Verheijen, A. Graff, M. Simon-Najasek, F. Altmann, M. Fiederle, and O. Ambacher, *Semicond. Sci. Technol.* **36**, 034003 (2021).
- ⁷²J. Casamento, H. G. Xing, and D. Jena, *Phys. Status Solidi B* **257**, 1900612 (2020).
- ⁷³J. Casamento, C. S. Chang, Y.-T. Shao, J. Wright, D. A. Muller, H. G. Xing, and D. Jena, *Appl. Phys. Lett.* **117**, 112101 (2020).
- ⁷⁴J. Casamento, V. Gund, H. Lee, K. Nomoto, T. Maeda, B. Davaji, M.-J. Asadi, J. Wright, Y.-T. Shao, D. A. Muller, A. Lal, H. G. Xing, and D. Jena, *arXiv:2105.10114* (2021).
- ⁷⁵P. Wang, D. Wang, N. M. Vu, T. Chiang, J. T. Heron, and Z. Mi, *Appl. Phys. Lett.* **118**, 223504 (2021).
- ⁷⁶Y. Cao and D. Jena, *Appl. Phys. Lett.* **90**, 182112 (2007).

Epitaxial $\text{Sc}_x\text{Al}_{1-x}\text{N}$ on GaN exhibits attractive High-K Dielectric Properties

Supplementary Information

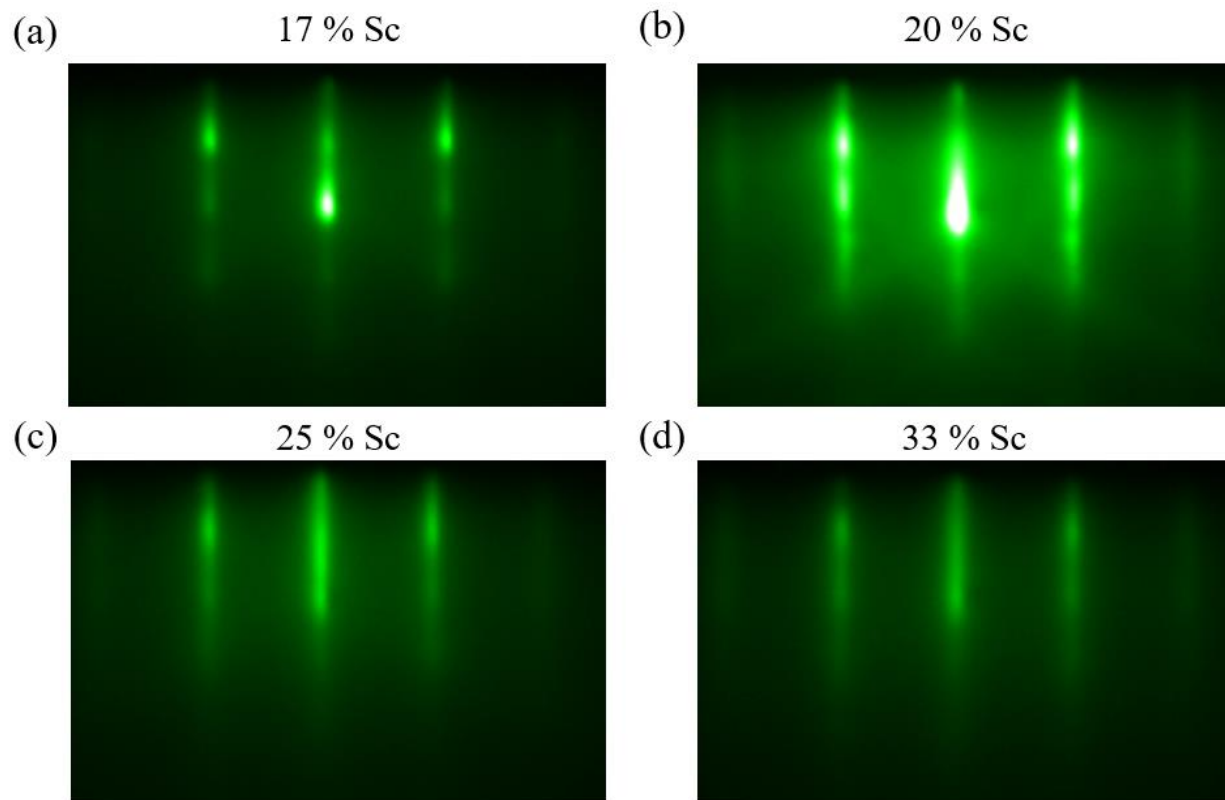


Figure S-1: (a-d) Reflection High Energy Electron Diffraction (RHEED) Images of $\text{Sc}_x\text{Al}_{1-x}\text{N}$ ($x = 0.17$ to 0.33) taken immediately after the growth.

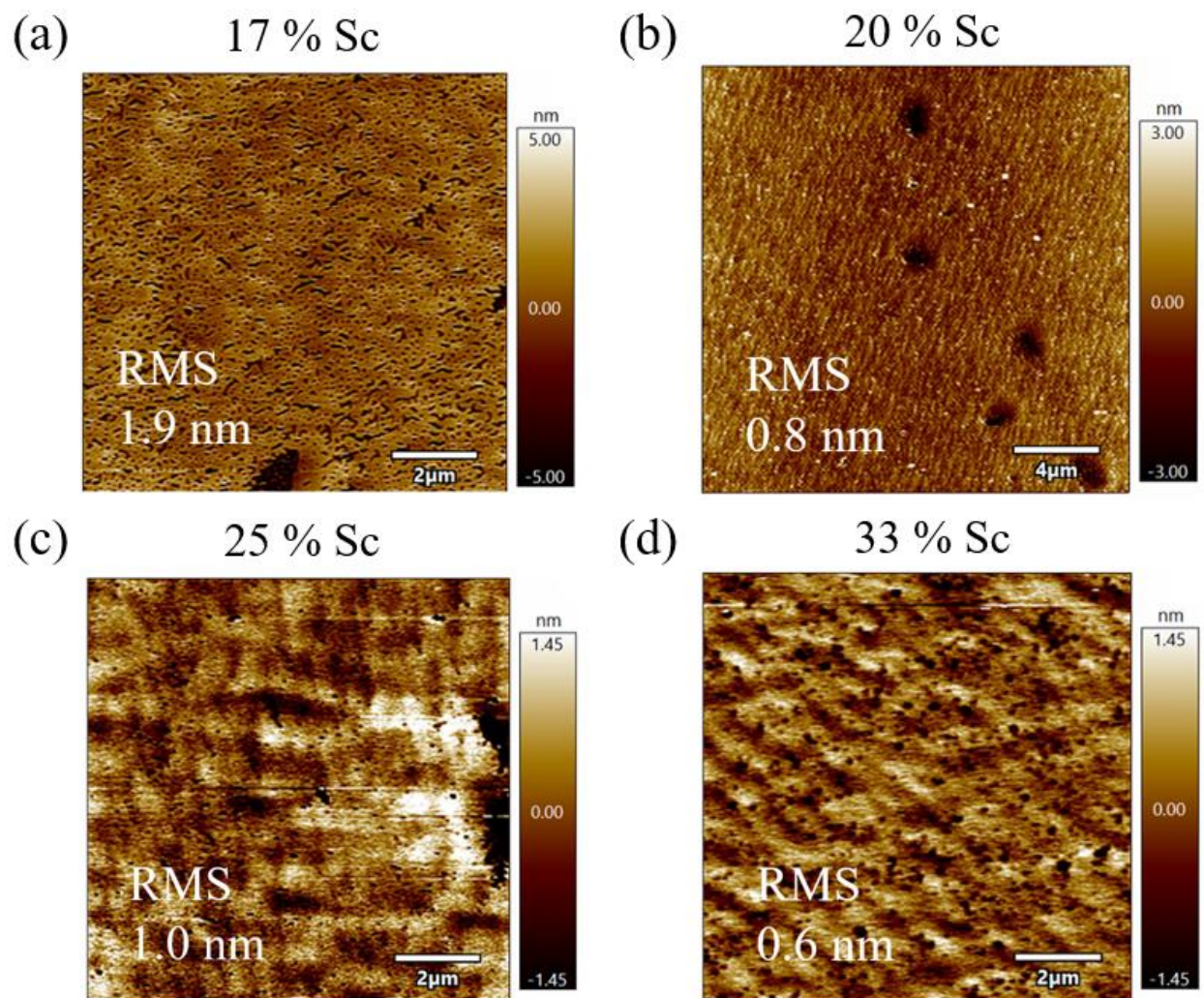


Figure S-2: (a-d) AFM Images of $\text{Sc}_x\text{Al}_{1-x}\text{N}$ ($x = 0.17$ to 0.33) taken after growth.